Mon. Not. R. Astron. Soc. **423,** 2753–2763 (2012) doi:10.1111/j.1365-2966.2012.21085.x

Extended X-ray emission from non-thermal sources in the COSMOS field: a detailed study of a large radio galaxy at $z = 1.168$

Vibor Jelić,[1⋆] Vernesa Smolčić,[2,3,4†] Alexis Finoguenov,[5,6] Masayuki Tanaka,[7] Francesca Civano,[8] Eva Schinnerer,[9] Nico Cappelluti[10] and Anton Koekemoer[11]

[1]*ASTRON, the Netherlands Institute for Radio Astronomy, PO Box 2, 7990 AA Dwingeloo, the Netherlands*
[2]*Argelander Institut for Astronomy, Auf dem Hügel 71, Bonn 53121, Germany*
[3]*European Southern Observatory, Karl-Schwarzschild-Strasse 2, 85748 Garching bei München, Germany*
[4]*Physics Department, University of Zagreb, Bijenička cesta 32, 10002 Zagreb, Croatia*
[5]*Max-Planck-Institut für extraterrestrische Physik, Giessenbachstrasse, 85748 Garching bei München, Germany*
[6]*Center for Space Science Technology, University of Maryland, Baltimore County, 1000 Hilltop Circle, Baltimore, MD 21250, USA*
[7]*Institute for the Physics and Mathematics of the Universe, The University of Tokyo, 5-1-5 Kashiwanoha, Kashiwa-shi, Chiba 277-8583, Japan*
[8]*Harvard-Smithsonian Centre for Astrophysics, 60 Garden Street, Cambridge, MA 02138, USA*
[9]*Max-Planck-Institut für Astronomie, Königstuhl 17, D-69117 Heidelberg, Germany*
[10]*INAF-Osservatorio Astronomico di Bologna, Via Ranzani 1, I-40127 Bologna, Italy*
[11]*Space Telescope Science Institute, 3700 San Martin Drive, Baltimore, MD 21218, USA*

Accepted 2012 April 10. Received 2012 April 10; in original form 2011 August 8

ABSTRACT

X-ray selected galaxy group samples are usually generated by searching for extended X-ray sources that reflect the thermal radiation of the intragroup medium. On the other hand, large radio galaxies that regularly occupy galaxy groups also emit in the X-ray window, and their contribution to X-ray selected group samples is still not well understood. In order to investigate their relative importance, we have carried out a systematic search for non-thermal extended X-ray sources in the Cosmic Evolution Survey (COSMOS) field. Based on the morphological coincidence of X-ray and radio extensions, out of 60 radio galaxies, and ∼300 extended X-ray sources, we find only one candidate where the observed extended X-ray emission arises from non-thermal processes related to radio galaxies. We present a detailed analysis of this source, and its environment. Our results yield that external inverse Compton emission of the lobes is the dominant process that generates the observed X-ray emission of our extended X-ray candidate, with a minor contribution from the gas of the galaxy group hosting the radio galaxy. Finally, we show that finding only one potential candidate in the COSMOS field (in a redshift range $0 < z < 6$ and with radio luminosity between 10^{25} and 10^{30} W Hz^{-1}) is consistent with expected X-ray counts arising from synchrotron lobes. This implies that these sources are not a prominent source of contamination in samples of X-ray selected clusters/groups, but they could potentially dominate the $z > 1$ cluster counts at the bright end ($S_X > 7 \times 10^{-15}$ erg s^{-1} cm^2).

Key words: radiation mechanisms: non-thermal – radiation mechanisms: thermal – surveys – galaxies: active – radio continuum: galaxies – X-rays: galaxies: clusters.

1 INTRODUCTION

Radio galaxies constitute the most powerful and the largest scale active galactic nuclei (AGN) phenomena. Their jets span distances of up to 1 Mpc. The optical hosts of powerful radio loud AGN usually have colours consistent with that of galaxies in the so-called 'green valley', i.e. a region in a colour versus stellar mass plane thought to reflect the evolutionary transition of blue-star-forming galaxies to red-and-dead ones (Smolčić 2009). They have a higher molecular gas content relative to less powerful radio galaxies inhabiting the red sequence (Smolčić & Riechers 2011). They often show signs of merger activity (Simpson & Rawlings 2002), and they usually reside in group environments (Baum, Heckman & van Breugel 1992). As their high brightness in the radio allows detections out to high redshift, powerful radio galaxies are often used as tracers of distant groups/clusters of galaxies.

⋆E-mail: jelic@astron.nl
†ESO ALMA COFUND fellow.

A direct, and powerful way to detect clusters and groups of galaxies is via extended X-ray emission reflecting thermal bremsstrahlung radiation from the cluster/group gas (i.e. intercluster/intragroup medium; ICM). With the advent of deep X-ray surveys, and the optimization of cluster/group-detection algorithms hundreds of faint X-ray clusters have been detected in such a way out to $z \sim 2$ (Finoguenov et al. 2007, 2009, 2010; Bielby et al. 2010; Henry et al. 2010; Tanaka, Finoguenov & Ueda 2010; Gobat et al. 2011). However, large radio galaxies, which are preferentially found in such galaxy groups/clusters, are also luminous in the X-rays, thus possibly biasing the X-ray cluster searches (see below). Furthermore, the X-ray emission of their jets, hotspots and lobes may outlive the radio emission, as inverse Compton (IC)–cosmic microwave background (CMB) emission can downgrade the electrons required for (high frequency) radio emission (Fabian et al. 2009; Mocz, Fabian & Blundell 2011).

It has been demonstrated that the X-ray emission of radio galaxies arises from three main processes: synchrotron radiation emitted by relativistic electrons, IC scattering of the synchrotron photons (so-called synchrotron self-Compton, SSC, process) or the CMB photons (so-called external Compton, EC, process) off the relativistic electrons. The first and second processes are predominant in jet-knots and hotspots of low-redshift radio galaxies, while the last process can regularly be associated with the extended lobes of radio galaxies (see Kataoka & Stawarz 2005 for details). It is important to note that the X-ray flux of EC emission is proportional to the energy density of the CMB photons that rises with redshift as $(1 + z)^4$. This rise in flux partially compensates the dimming effect due to the large distances to such sources (Felten & Rees 1969; Schwartz 2002), thereby making them detectable also at high redshifts ($z \gtrsim 1$; e.g. Simpson & Rawlings 2002; Fabian et al. 2003; Blundell et al. 2006; Johnson et al. 2007; Erlund, Fabian & Blundell 2008).

Depending on the expected number of extended X-ray-emitting radio lobe sources (via EC), they might be a serious contaminant in deep X-ray surveys searching for clusters/groups at high redshifts. Assuming that radio AGN emit in the X-ray via EC emission, and evolving radio AGN luminosity functions (LFs) Celotti & Fabian (2004) argued that at redshifts of $z \gtrsim 1$ the EC emission of radio lobes will likely dominate in X-rays (at $L_{\rm X} > 10^{44}\,{\rm erg\,s^{-1}}$) over the thermal gas emission of the clusters/groups. When, however, a radio galaxy lies in a cluster/group, the total X-ray emission from this system is likely a combination of EC emission from the radio lobes of the galaxy, and thermal bremsstrahlung emission from the cluster/group gas. However, so far there has been just a single survey (Finoguenov et al. 2010) that tried to quantify that. Finoguenov et al. (2010) searched for X-ray galaxy clusters in the Subaru-*XMM Deep Field* (SXDF), covering $1.3\,{\rm deg^2}$. They identified 57 cluster candidates, four of which they consider likely EC X-ray sources and two more which are likely a combination of EC scattering and thermal cluster emission.

In order to put stronger constraints on extended X-ray sources due to non-thermal processes in deep X-ray surveys, here we present a search for EC-dominated X-ray candidates in the Cosmic Evolution Survey (COSMOS; Scoville et al. 2007) field, and discuss their expected abundance in future X-ray surveys. The paper is organized as follows. In Section 2 we give a brief overview of the COSMOS survey and the data used for this work. In Section 3 we describe our systematic search for EC-dominated X-ray sources in the COSMOS field. The radio, X-ray and optical properties of our single candidate are presented in Section 4, while the properties of the associated galaxy group are discussed in Section 5. The origin of observed X-ray emission is discussed in Section 6. Section 7 presents predictions for EC-dominated X-ray sources in future X-ray surveys. We conclude the paper with Section 8.

Throughout we assume Λ cold dark matter (ΛCDM) cosmology with 7-year *Wilkinson Microwave Anisotropy Probe* (*WMAP*7) parameters (Komatsu et al. 2011): $h = 0.71$, $\Omega_{\rm b} = 0.045$, $\Omega_{\rm m} = 0.27$ and $\Omega_\Lambda = 0.73$, and we use AB magnitude system.

2 DATA

The COSMOS survey is designed to probe the formation and evolution of galaxies as a function of cosmic time and large-scale structure environment. The survey covers a $2\,{\rm deg^2}$ area close to celestial equator (Scoville et al. 2007) with multiwavelength imaging from X-ray to radio wavelengths, including *Hubble Space Telescope* (*HST*)/Advanced Camera for Surveys (ACS) imaging (see Koekemoer et al. 2007) and optical spectroscopy (*z*COSMOS; Lilly et al. 2007, 2009). Because of this broad wavelength coverage the photometric redshifts for galaxies in the COSMOS field are determined to an excellent accuracy of $0.007(1 + z)$ for $i^+ < 22.5$ (Ilbert et al. 2009; Salvato et al. 2009). The stellar masses of every source in the photometric redshift catalogue are estimated using a Salpeter initial mass function (IMF).

In radio wavelengths, the COSMOS field has been observed at 1.4 GHz [Very Large Area (VLA)-COSMOS survey; Schinnerer et al. 2007, 2010] and 327 MHz (Smolčić et al., in preparation) with the National Radio Astronomy Observatory (NRAO) VLA in A and C configurations. The reached rms and resolution at 327 MHz (1.4 GHz) are $\sim$0.4 mJy beam^{-1} ($\sim$8 μJy beam^{-1}) and $6.0 \times 5.4\,{\rm arcsec^2}$ ($1.5 \times 1.4\,{\rm arcsec^2}$), respectively. The 1.4-GHz catalogue utilized here contains $\sim$2400 ($\geq 5\sigma$) sources, 60 of which are radio galaxies (with clear core/jet/lobe features).

X-ray observations of the COSMOS field have been performed both with *XMM–Newton* (1.5 Ms covering $2\,{\rm deg^2}$; Hasinger et al. 2007) and *Chandra* (1.8 Ms covering inner $1\,{\rm deg^2}$; Elvis et al. 2009). Based on a composite mosaic of both observations, a galaxy group catalogue has been generated (Finoguenov et al. 2007; Finoguenov et al., in preparation). It contains $\sim$300 extended sources out to redshifts of 1.3 with total masses within a radius at 200 times the critical density in the range of $M_{200} \in [7 \times 10^{12}, 3 \times 10^{14}]\,{\rm M_\odot}$. The extended X-ray source detection is based on a wavelet analysis technique and includes removal of point sources (Finoguenov et al. 2009). Each X-ray cluster candidate has been further independently verified via an optical galaxy cluster search (making use of both the COSMOS photometric and spectroscopic redshifts, following the procedure outlined in Finoguenov et al. 2010).

3 SEARCH FOR JOINT RADIO/X-RAY CO-EXISTANCE IN THE COSMOS FIELD

Using the data mentioned in Section 2, we carried out a systematic search for EC-dominated X-ray sources. The search is based on the coincidence of radio and X-ray emissions. We compare the centring and positional angle of each of the 60 morphologically complex radio sources drawn from the 20 cm VLA-COSMOS catalogue with the associated extended X-ray emission in the 0.5–2 keV band. To avoid a possible identification bias towards availability of an optical counterpart no prior on either source has been applied.

In addition to a positional match, a coincidence in elongation of radio and X-ray emissions (to within 10°) is required by the method. This creates a robust identification of the extended X-ray source as a counterpart of radio lobes, as the chance probability of such an alignment is 10^{-4}, given the density of both X-ray and radio

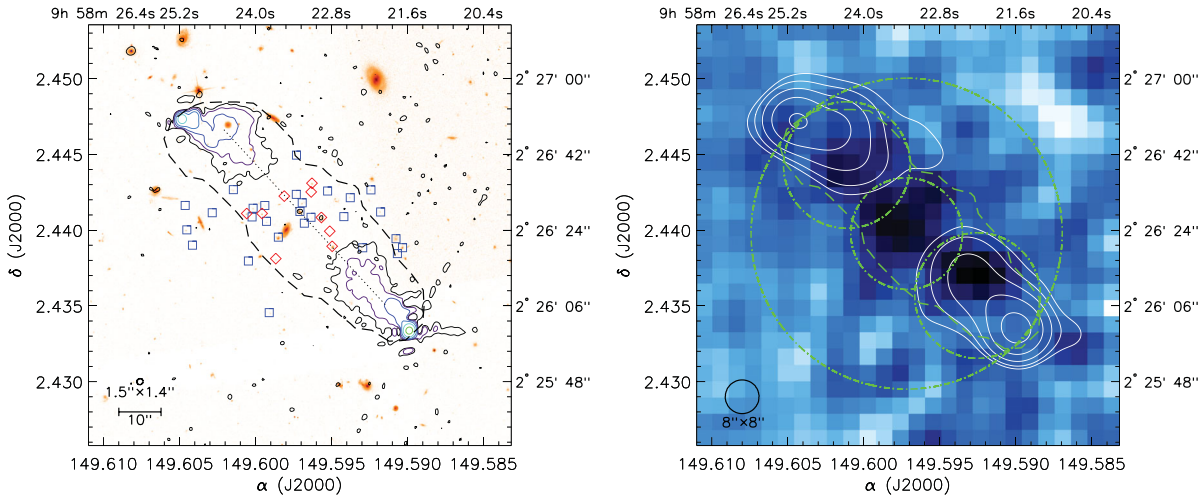

Figure 1. Multiwavelength image of the region around the EC-dominated X-ray candidate. Left: *HST*-ACS *i*-band image is presented in a red scale. The radio emission of the associated radio galaxy at 1.4 GHz is plotted with solid $3^i\sigma$ level contours (where $i = 1, 2, \ldots$ and $\sigma = 17.16\,\mu\mathrm{Jy\,beam^{-1}}$). The synthesized beam of the radio image is $1.5 \times 1.4\,\mathrm{arcsec}^2$ (thick solid ellipse plotted in the bottom left-hand corner). Borders of extended X-ray emission obtained by the wavelet analysis of the *XMM–Newton* image are shown by the dashed line. Associated optical/IR galaxies identified via the Voronoi method are marked with blue boxes and red diamonds, according to their $i - K_s$ colour (see Section 5). Right: *XMM–Newton*, background point source subtracted and smoothed to $8 \times 8\,\mathrm{arcsec}^2$ resolution, image of the region around the EC-dominated X-ray candidate (presented in a blue scale; note that darker colours show regions with stronger X-ray emission). The radio emission at 1.4 GHz is smoothed to the resolution of the X-ray image and overplotted as solid white contours. A dashed green line marks the X-ray flux extraction region associated with the extended X-ray emission, while the dash–dotted green circles are regions associated with the core, lobes and a putative group emission.

sources, and chance alignment of principal axes. However, such a search is limited to the early phase of radio activity and may not select X-ray only lobes. Compared to a similar study done on the 1.3 deg^2 of SXDF survey (Finoguenov et al. 2010), we find just one EC-dominated X-ray candidate (Fig. 1), which implies a factor of 6 lower frequency of the phenomenon as inferred by Finoguenov et al. (2010). We note that the redshift of the COSMOS source, $z_{\mathrm{spec}} = 1.168$, is at a similar redshift as the brightest EC-dominated X-ray candidate in SXDF.

Hereafter, we refer to this system as the EC-dominated X-ray candidate. Its radio, X-ray and optical properties are presented in the following section.

4 EC-DOMINATED X-RAY CANDIDATE

4.1 X-ray properties

The extended X-ray emission associated with our candidate has been identified using the full *XMM–Newton* survey of the COSMOS field (it is outside the area covered by *Chandra*). However, the best imaging quality is available in the observation 0203362201, which has a 26 ks cleaned exposure and the object is located next to the telescope optical axis (best point spread function, PSF, and sensitivity). We show the X-ray counts, smoothed to $8 \times 8\,\mathrm{arcsec}^2$ resolution, in Fig. 1. From the figure it is obvious that the X-ray emission is arising from the region associated with the radio galaxy. The emission shows both unresolved and resolved components with a total flux of $(3.6 \pm 1.2) \times 10^{-15}\,\mathrm{erg\,s^{-1}\,cm^{-2}}$ in the observed 0.5–2 keV band (dashed line in left-hand panel of Fig. 1).

In order to get a better insight into the X-ray properties associated with the source, we have extracted the counts from three zones within the X-ray map. These zones, illustrated by the dash–dotted green areas in the right-hand panel of Fig. 1, encompass the core, both lobes and a putative group emission. Using both the stowed background and the local background region, selected from the same chip, but 2 arcmin away from the source, we analysed the spectra in the 0.4–7.5 keV range for each zone separately. Significant detections have been obtained in all three zones. Using the *XMM* PSF model, and for the putative group emission an assumption of azimuthal symmetry, we have solved for intrinsic flux of all these components: in the observed 0.5–2 keV band and in units of $10^{-15}\,\mathrm{erg\,s^{-1}\,cm^{-2}}$ the lobe emission amounts to 2.7 ± 0.7, core emission to 1.7 ± 0.4, total group emission of 1.4 ± 1.2 and its contribution to the lobes is 0.5 ± 0.4. The group component has not been significantly detected. In Fig. 2 we show the spectrum of the lobes. Given the marginal contribution of the group emission, established above, we ignored it, finding a photon index of 2.6 ± 0.5 ($\chi^2 = 3.2/7$ dof). The core shows a hard spectrum with a photon index of 0.6 ± 0.4.

4.2 Radio properties

The radio counterpart of the EC-dominated X-ray candidate is identified as a large powerful radio galaxy J095822.93+022619.8 with integrated source flux density of $S_{1.4\,\mathrm{GHz}} = (112.9 \pm 0.5)$ mJy (Schinnerer et al. 2007) and $S_{327\,\mathrm{MHz}} = (470.6 \pm 0.5)$ mJy (Smolčić et al., in preparation). The spectroscopic redshift of its optical counterpart is 1.1684 ± 0.0007 (see Section 4.3), which corresponds to a luminosity distance of $d_L = 8062$ Mpc for the adopted cosmology. Thus, the monochromatic radio powers of the source at 1.4 GHz and 327 MHz are $L_{1.4\,\mathrm{GHz}} = 8.8 \times 10^{26}\,\mathrm{W\,Hz^{-1}}$ and $L_{327\,\mathrm{MHz}} = 3.7 \times 10^{27}\,\mathrm{W\,Hz^{-1}}$, respectively.

Morphologically, the source shows a structure of Fanaroff–Riley (FR) class II (Fanaroff & Riley 1974), i.e. a luminous radio galaxies with predominant emission from the lobes (see Fig. 1 and Table 1). The radio emission of the jets themselves is not detected. The radio core, located centrally between the lobes (see the line joining the lobes in Fig. 1), is detected at $\sim 4\sigma$ in the 1.4-GHz radio map. The central parts of the lobes are ~26.5 arcsec (~220 kpc) away from the core in two diametrically opposite directions

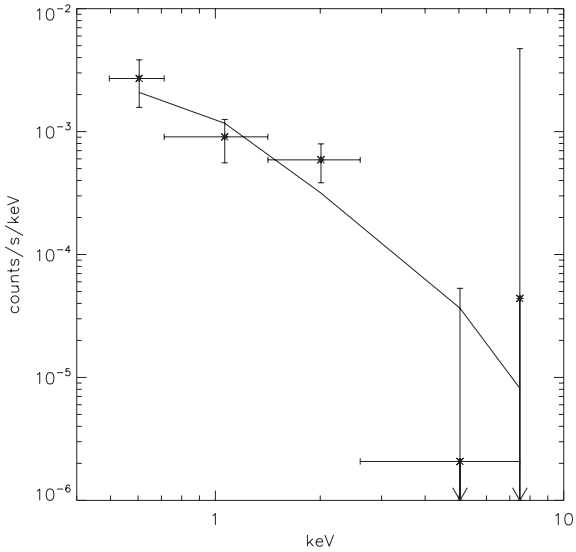

Figure 2. Fitted power-law spectrum of the X-ray emission in the 0.4–10 keV range using both the stowed background and the local background. Data points are given for the X-ray emission associated with the lobes (see Fig. 1). Note that the spectral shape is hard, which is consistent with the non-thermal emission from EC scattering, rather than thermal emission arising from the galaxy group.

Table 1. Integrated flux density and projected angular size of morphological features resolved in the 1.4-GHz radio map.

Morphological features	$S_{1.4\,\mathrm{GHz}}$ (mJy)	Angular size (arcsec^2)
NE hotspot	19.5 ± 0.5	1.5×1.4
SW hotspot	35.3 ± 0.5	1.5×1.4
NE lobe	36.2 ± 0.5	23.5×16.4
SW lobe	21.9 ± 0.5	24.1×14.3

[north-east(NE)–south-west(SW) direction on the plane of the sky]. The hotspot of the NE lobe is off the joint line between the lobes, suggesting interaction with a medium.

Combining the images at 327 MHz and 1.4 GHz, the spectral index map of the source is obtained (see Fig. 3; $S_\nu \propto \nu^{\alpha_r}$). Prior to the spectral index calculation (i) the 1.4-GHz image was convolved and re-gridded to match the resolution and pixel scale of the 327-MHz image, (ii) positional alignment between the two images was checked using 45 point sources (Smolčić et al., in preparation) and (iii) pixels with values below 3σ in each image were blanked. The spectral index shows the expected behaviour for both lobes. It steepens radially towards the core from -0.6 to -1.5. The average spectral index is $\alpha_r = -(1.0 \pm 0.2)$. For clarity, we also calculate the spectral index from the integrated flux density of the source at 327 MHz and 1.4 GHz, obtaining $\alpha_r = \log(S_{\nu_2}/S_{\nu_1})/\log(\nu_2/\nu_1) = -0.98$, which is in agreement with the result obtained from the spectral index map. Throughout the paper we will use $\alpha_r = -(1.0 \pm 0.2)$ as the average spectral index of the lobes and $\alpha_r = -(0.7 \pm 0.2)$ as the average spectral index of the hotspots.

The total radio luminosity of the source, obtained by integrating the synchrotron spectrum from 1 MHz to 100 GHz (e.g. equation 1 in Smolčić et al. 2007), is $L_\mathrm{r} = 6.7 \times 10^{38}$ W.

4.2.1 *Magnetic field strength in the lobes and hotspots*

Based on the obtained radio properties of our source, we estimate the magnetic field strength in its lobes and hotspots. This will be further used to estimate the expected IC emission (Section 6.1).

We follow Smolčić et al. (2007) and apply the minimum energy condition. Briefly, the minimum energy condition corresponds almost to equipartition between the relativistic particles (protons and electrons, $E_\mathrm{p,e}$) and the magnetic field, E_{B_eq} (for details see Pacholczyk 1970). The magnetic field strength is then given by (e.g. Miley 1980)

$$B_\mathrm{eq} = 5.69 \times 10^{-5} \left(\frac{1+k}{\eta} \frac{S_\mathrm{r}(1+z)^{3-\alpha_r}}{\nu^{\alpha_r}\theta_x\theta_y s} \times \frac{\nu_2^{\alpha_r+1/2} - \nu_1^{\alpha_r+1/2}}{\alpha_r + \frac{1}{2}} \right)^{2/7} \mathrm{G}, \quad (1)$$

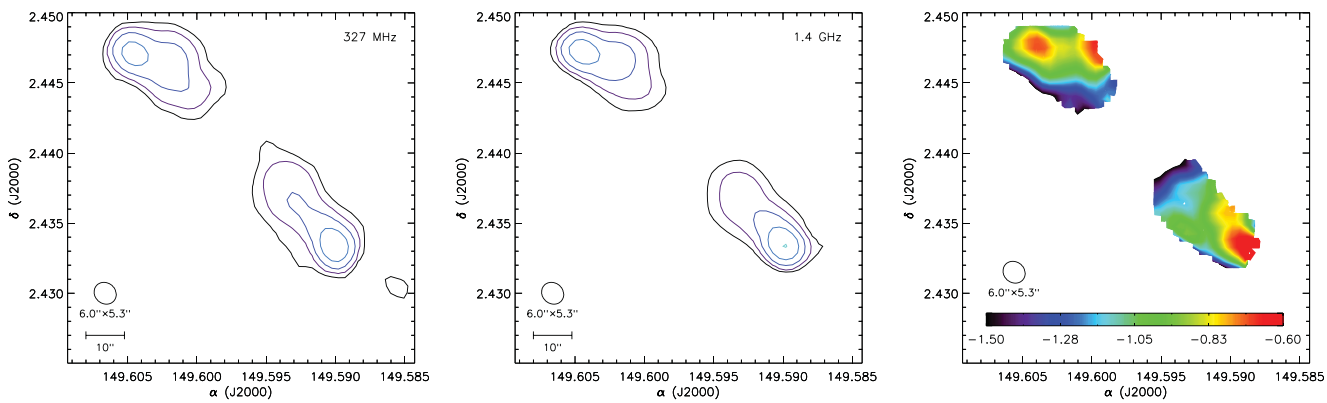

Figure 3. The radio emission of the associated radio galaxy at 327 MHz (left), at 1.4 GHz (middle) convolved to the resolution of the 327 MHz image and the corresponding spectral index map of the radio emission ($S_\nu \propto \nu^{\alpha_r}$; right). Contours of the radio emission have $3^i\sigma$ levels, where $i = 1, 2, \ldots$, $\sigma_{327\,\mathrm{MHz}} = 0.4$ mJy beam^{-1}, and $\sigma_{1.4\,\mathrm{GHz}} = 0.14$ mJy beam^{-1}. The synthesized beams of the radio images are 6.0×5.4 arcsec^2 (thick solid ellipses plotted in the bottom left-hand corner of the images). As expected, the spectral index steepens radially towards the core. The average spectral index of both lobes together is $\alpha_r = -(1.0 \pm 0.2)$. By comparing the spectral index map with the X-ray emission shown in Fig. 1, we note that the X-ray emission stems from the zones of steeper spectral indexes.

where z is the redshift of the source, S_r (Jy) is the observed radio flux of the emitting region at frequency ν_r (GHz), $\theta_{x,y}$ (arcsec) is the angular size of the emitting region, s (kpc) is the path length through the source along the line of sight, $\nu_{1,2}$ (GHz) are lower and upper frequency cut-offs and α_r is the spectral index. Equation (1) assumes (i) a cylindrical symmetry of the lobes, (ii) equal energy densities carried by protons and electrons in the lobes ($k = 1$), (iii) no relativistic beaming ($\delta = 1$), (iv) the volume of the lobes to be completely filled with the plasma ($\eta = 1$) and (v) the magnetic field is transverse to the line of sight ($\sin\Phi = 1$). Given the averaged properties of the lobes ($S_{1.4\,\mathrm{GHz}} = (29.0 \pm 0.5)$ mJy, $\alpha_r = -(1.0 \pm 0.2)$, $\theta_x = 23.8$ arcsec, $\theta_y = 15.35$ arcsec and $s = 130$ kpc) and taking 1 MHz and 100 GHz for $\nu_{1,2}$, the obtained magnetic field strength is $B_{\mathrm{eq}} = (10 \pm 2)\,\mu$G. The magnetic energy density is $u_B = B_{\mathrm{eq}}^2/8\pi = (4.0 \pm 1.5) \times 10^{-12}\,\mathrm{erg\,cm^{-3}}$. The errors are propagated from uncertainties on $S_{1.4\,\mathrm{GHz}}$, α_r and z.

Given the averaged properties of the hotspots ($S_{1.4\,\mathrm{GHz}} = (27.4 \pm 0.5)$ mJy, $\alpha_r = -(0.7 \pm 0.2)$, $\theta_x = 1.4$ arcsec, $\theta_y = 1.5$ arcsec and $s = 12$ kpc) and taking 1 MHz and 100 GHz for $\nu_{1,2}$, the obtained magnetic field strength is $B_{\mathrm{eq}} = (53 \pm 2)\,\mu$G and the magnetic energy density is $u_B = B_{\mathrm{eq}}^2/8\pi = (113 \pm 8) \times 10^{-12}\,\mathrm{erg\,cm^{-3}}$.

4.3 Optical properties

The radio core of the large radio galaxy is associated with an optical source located at $\alpha = 9^{\mathrm{h}}58^{\mathrm{m}}23\overset{\mathrm{s}}{.}31$, $\delta = +02^{\circ}26'28\overset{''}{.}33$ (see Fig. 4).

In the *HST*-ACS image (Koekemoer et al. 2007), with a pixel scale of 0.03 arcsec pixel^{-1}, two central cores are clearly visible (see Fig. 4). The separation of the cores is 0.22 arcsec, which corresponds to a physical distance of ∼1.7 kpc at the redshift of the source. The presence of two cores could be either interpreted as the two nuclei of merging galaxies or as two star formation regions in a single galaxy. Alternatively, they are a superposition of two nuclei of two independent galaxies in the same group. Given the average density in the group selected by Voronoi tessellation (see Section 5; 2.68×10^5 galaxies per deg^2), such a probability is, however, small, i.e. $P = 3.2 \times 10^{-3}$.

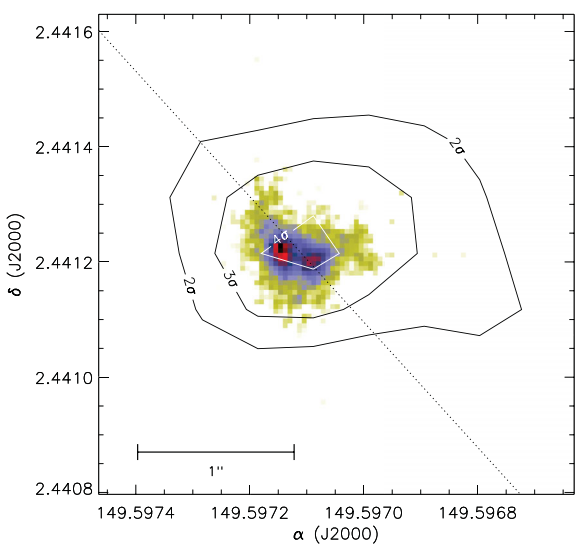

Figure 4. *HST*-ACS *i*-band image of the region around the radio core of the EC-dominated X-ray candidate. The radio emission at 1.4 GHz is plotted with solid contours ($\sigma = 17.16\,\mu$Jy beam^{-1}). The synthesized beam of the radio image is 1.5×1.4 arcsec^2.

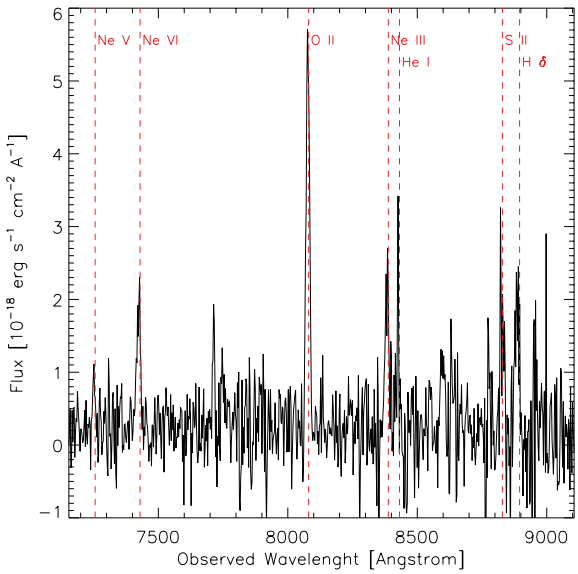

Figure 5. A part of the optical spectrum of the source taken within the *z*COSMOS survey. The spectroscopic redshift is 1.1684 ± 0.0007, and given the presence of only narrow lines ([Ne V] doublet and [O II]), the source is classified as a narrow line emission galaxy.

An optical spectrum (5500–9500 Å) of the source has been taken within the *z*COSMOS survey (Lilly et al. 2007, 2009). The *z*COSMOS slit was oriented north–south, with the dispersion axis in east–west direction. The spectroscopic redshift is 1.1684 ± 0.0007, and given the presence of only narrow lines ([Ne V] doublet at 3346 and 3426 Å and [O II] at 3727 Å, see Fig. 5), the source is classified as a narrow line emission galaxy. Given the redshift of the source, it is not possible to use a diagnostic diagram (Kewley et al. 2001; Lamareille et al. 2004) to classify the ionizing source (nuclear versus star formation). We analysed the optical spectrum to look for two emission line systems corresponding to the two optical cores in the *HST*-ACS image. Fitting the [Ne V] emission line at 3426 Å, two peaks in the line profile are visible with a separation comparable to the *z*COSMOS spectral resolution (∼600). In this case, the spectroscopic data available are not sufficient to draw firm conclusions on the nature of the two optical cores. The north–south separation of the two cores is 0.1 arcsec, so given the angular resolution of *z*COSMOS (0.20 arcsec pixel^{-1}), it is not possible to spatially resolve the two sources in the 2D spectrum either.

5 PROPERTIES OF THE ASSOCIATED GALAXY GROUP

To determine whether an optical galaxy overdensity is associated with the X-ray-emitting lobe candidate, we apply a Voronoi tessellation analysis (e.g. Ebeling & Wiedenmann 1993) to the field surrounding our radio galaxy to identify potential galaxy group members. The strength of the method is that no a priori assumptions need to be made about cluster/group properties, making the technique sensitive to non-symmetric (e.g. elongated) structures (see e.g. Smolčić et al. 2007; Oklopčić et al. 2010). We first select galaxies within ∼20 arcmin (corresponding to 10 Mpc physical distance at $z = 1.1$) from the radio galaxy that have photometric redshifts within $\Delta z = 3\sigma_{\delta z}(1 + z_0)$ relative to the redshift of the radio galaxy ($z_0 = 1.168$). Following Ilbert et al. (2009) we take $\sigma_{\delta z} = 0.007$ and 0.034 for galaxies with $i^+ < 22.5$ and 26.5, respectively. Note that only one spectroscopic redshift (i.e. that of

the radio galaxy host) is available in the redshift range and area of interest.

The Voronoi tessellation method considers the selected galaxies as a two-dimensional distribution of points (called nuclei) on a plane of the sky. The plane is then subdivided into polygonal regions such that a surface area of each region is minimized and contains only one nucleus. Since the inverse of the resulting surface area of each region corresponds to the effective local density of the galaxy, one can identify overdensities and therefore clustering of galaxies.

Once we compute the Voronoi regions, we estimate the background density via Monte Carlo simulations (Botzler et al. 2004; Smolčić et al. 2007; Oklopčić et al. 2010). The same sample of galaxies is 100 times randomly redistributed over the same area. The Voronoi tessellation is then applied to each generated field, and the mean local density ($\bar{\rho}_{\rm bg}$) and its standard deviation ($\sigma_{\rm bg}$) are calculated. All Voronoi regions with densities $\rho \geq \bar{\rho}_{\rm bg} + 10\sigma_{\rm bg}$ are considered as overdensities. Note that we performed the Voronoi tessellation analysis on a much larger region than the expected group/cluster area to facilitate the identification of overdensities.

The results of the Voronoi tessellation analysis, shown in Fig. 6, reveal a clear galaxy overdensity around the radio galaxy, extending over ∼300 kpc. We identify 37 galaxies in the overdensity. Their redshift and spatial distribution, as well as the $i - K_{\rm s}$ versus $K_{\rm s}$ colour–magnitude diagram (CMD) are shown in Fig. 7. In the CMD we also show the expected red sequence at $z = 1.168$. We use the Bruzual & Charlot (2003) population synthesis code with an updated treatment of thermally pulsating asymptotic giant branch (AGB) stars. We fitted the red sequence in nearby clusters (Bower, Lucey & Ellis 1992) with single burst models formed at $z = 5$ and varying metallicity. We then evolved the sequence back over time to $z = 1.16$.

Both a red sequence, and a blue cloud are discernible from the data. The brightest red sequence galaxy, which is also the most massive galaxy in the system ($M_* = 2.5 \times 10^{11}\,{\rm M}_\odot$), is located close to the centre of the overdensity. The host of the radio galaxy is the third brightest galaxy, and it has a green (i.e. intermediate between red and blue) colour. Such a colour is consistent with that expected for powerful radio galaxies (Smolčić et al. 2009) that often show signs of galaxy–galaxy mergers (e.g. Baum et al. 1992; Baldi & Capetti 2008, see also Section 4.3).

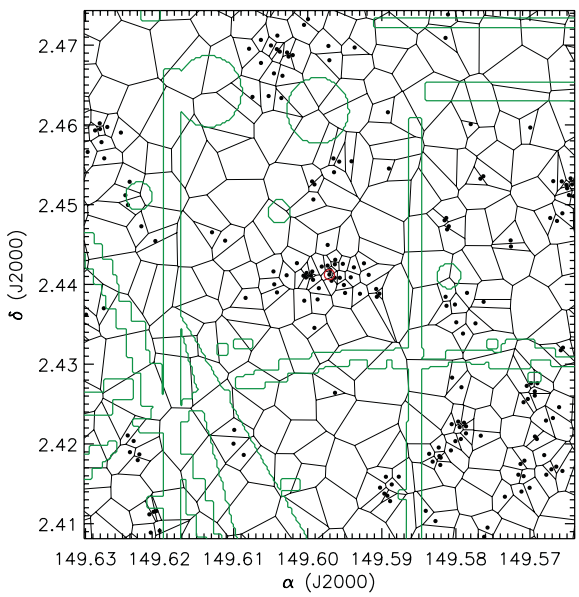

Figure 6. Voronoi tessellation in the area of the EC-dominated X-ray candidate. The candidate is marked with the red circle, while the galaxies from the photo-z catalogue are shown as black dots. Green regions correspond to masked-out regions around saturated object in the images used for the photo-z catalogue. We have identified 37 galaxies in the immediate surroundings of the X-ray-emitting lobe candidate.

In order to investigate the spatial distribution of different types of galaxies in the identified overdensity we divide the galaxies into red ($i - K_{\rm s} \geq 2$) and blue ($i - K_{\rm s} < 2$) galaxies. The first can be considered to be old passive galaxies with higher stellar masses ($\langle M_* \rangle \approx 2 \times 10^{10}\,{\rm M}_\odot$), while the latter are younger galaxies with likely ongoing star formation and on average lower stellar masses ($\langle M_* \rangle \approx 5 \times 10^{9}\,{\rm M}_\odot$). As shown in Fig. 7 there is no structured distribution that would be expected for relaxed groups or clusters (i.e. centrally concentrated massive red galaxies with less massive blue galaxies at the outskirts). The massive red galaxies are rather spread over the system, with possible higher clustering in two clumps, (i) surrounding the brightest and most massive galaxy, and (ii) to the east of the brightest galaxy where an agglomeration of five red galaxies is present. Such properties suggest a non-relaxed state of the system, i.e. an agglomeration of galaxies in the process of forming a relaxed group/cluster. Summing up the stellar masses of all galaxies identified in the overdensity we find a total stellar mass of $10^{12}\,{\rm M}_\odot$. We conclude that the identified system is likely a dynamically young group in the process of relaxation.

6 WHAT CAUSES THE X-RAY EMISSION?

In order to reveal the origin of the X-ray emission of the EC-dominated X-ray candidate, in this section we calculate the expected X-ray fluxes arising from the radio lobes and hotspots, and separately from the gas of the optically identified group. We discuss the implications of the results in Section 6.4.

There are two processes involving IC scattering that can result in X-ray emission from a radio source: (i) SSC emission, which results from IC scattering of synchrotron radiation by the same relativistic electrons that produce the synchrotron radiation; and (ii) IC scattering of CMB photons on synchrotron-emitting electrons (EC). In the high-luminosity hotspots, where the electron density is high, the dominant process is usually SSC (Hardcastle et al. 2004). However, low-luminosity hotspots show X-ray emission that is much brighter than would be expected by SSC process indicating addition component of the X-ray emission (Hardcastle et al. 2004). In the lobes the electron density is much lower than in the hotspots, so EC scattering typically dominates over SSC (Croston et al. 2004, 2005; Kataoka & Stawarz 2005).

6.1 IC scattering in the radio lobes

To estimate the EC emission coming from the lobes, we follow Kataoka & Stawarz (2005) and make the following assumptions: (i) the minimum energy condition; (ii) lobes have a cylindrical shape with radius R and length l; (iii) equal energy densities carried by protons and electrons in the lobes ($k = 1$); (iv) no relativistic beaming ($\delta = 1$) and (v) the volume of the lobes to be completely filled with the plasma ($\eta = 1$). Then, we write the ratio between the radio and EC X-ray luminosity, which equals to the ratio between the CMB photon energy density and the magnetic field energy density (both calculated in the rest frame of the emitting region), i.e. $L_{\rm EC}/L_{\rm r} \simeq u_{\rm CMB}/u_B$ (e.g. Rybicki & Lightman 1986). The CMB

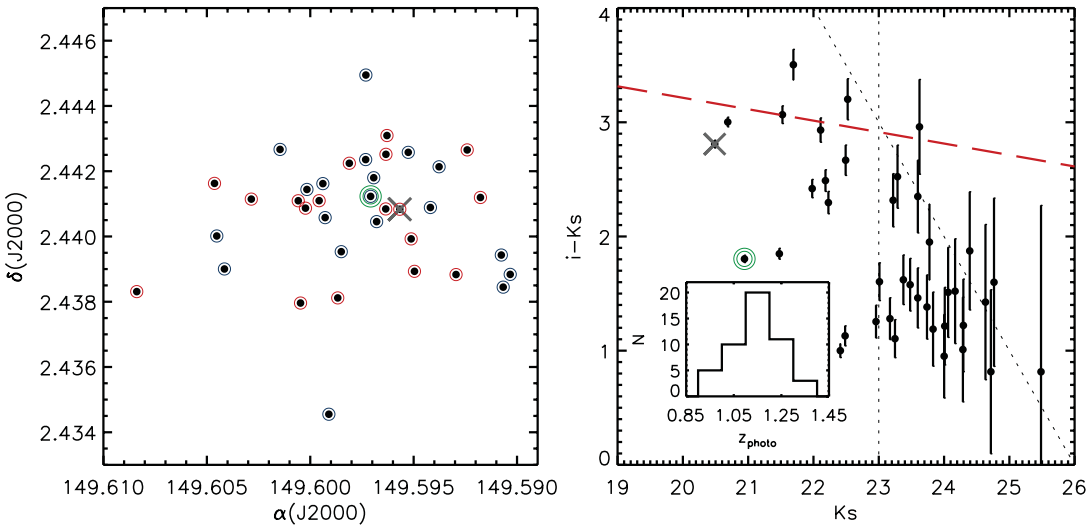

Figure 7. Spatial distribution of the galaxies in the overdensity identified via a Voronoi tessellation analysis (left-hand panel). Red ($i - K_s \geq 2$) and blue ($i - K_s < 2$) galaxies are also indicated. The right-hand panel shows the $i - K_s$ versus K_s CMD of the overdensity galaxies. A model red sequence expected at the group's redshift is shown by the dashed line (see text for details). The completeness limit in K_s (23 mag; vertical dotted line) and $i - K_s$ colour (inclined dotted line) are also shown. The brightest galaxy in the system is indicated with a cross, the optical host of the radio galaxy is circled by a double line. The photometric redshift distribution of the galaxies associated with the overdensity is shown in the inset.

Table 2. Observed X-ray flux of the EC-dominated X-ray candidate compared with expected fluxes of IC emission of the hotspots and lobes (see Sections 6.1 and 6.2), and thermal emission of the group (see Section 6.3).

	Observables				Derived properties	
	$S_{1.4\,\mathrm{GHz}}$ (mJy)	α_r	$S_{0.5-2\,\mathrm{keV}}$ (10^{-15} erg s^{-1} cm^{-2})	α_X	B_{eq} (μG)	$S_{0.5-2\,\mathrm{keV}}$ (10^{-15} erg s^{-1} cm^{-2})
Radio lobes	58.1 ± 0.5	$-(1.0 \pm 0.2)$	2.7 ± 0.7	$-(1.6 \pm 0.5)$	10 ± 2	$(2.5 \pm 0.5)_{EC}$
Radio hotspots	54.8 ± 0.5	$-(0.7 \pm 0.2)$			53 ± 2	$(0.04 \pm 0.01)_{SSC\,+EC}$
Associated group			1.4 ± 1.2			$(0.4 \pm 0.1)_{thermal}$

photon energy density in the rest frame is $u_{CMB} = 4.1 \times 10^{-13}(1 + z)^4$ erg cm^{-3} (e.g. Kataoka & Stawarz 2005) and u_B is calculated in Section 4.2.1.

However, to be able to compare the predicted EC emission with the observed X-ray emission, we need to estimate the flux arising from the EC process in the observed 0.5–2 keV band. In the EC process, electrons upscatter CMB photons to frequencies peaked at ν_{EC}, which is, in the Thomson regime and the frame of observer, given by (e.g. Rybicki & Lightman 1986; Wilson, Rohlfs & Hüttemeister 2009)

$$\nu_{EC} = \frac{4}{3}\gamma^2 \nu_{CMB}(1 + z)^{-1}, \tag{2}$$

where $\nu_{CMB} = 1.6 \times 10^{11}(1 + z)$ (Hz) is the frequency of the CMB photons, and

$$\gamma = \sqrt{\frac{2\pi m_e c}{e}\frac{\nu_r(1 + z)}{B}} \tag{3}$$

is the Lorenz factor of electrons emitting synchrotron radiation at frequency ν_r ($m_e = 9.109 \times 10^{-31}$ kg is the electron mass and $e = 1.602 \times 10^{-19}$ C is the elementary charge). Then, assuming a power law with a spectral index $\alpha_X \simeq \alpha_r$ (see Section 4.2), we calculate the X-ray flux, S_X, at frequency ν_X, by extrapolating the flux S_{EC} at frequency ν_{EC} (Stawarz, Sikora & Ostrowski 2003):

$$\frac{L_{EC}}{L_r} = \frac{\nu_{EC} S_{EC}}{\nu_r S_r} = \frac{\nu_X S_X}{\nu_r S_r}\left(\frac{\nu_{EC}}{\nu_X}\right)^{1+\alpha_r} \simeq \frac{u_{CMB}}{u_B}, \tag{4}$$

where S_r is the observed radio flux at frequency ν_r. Finally, we integrate S_X obtained from equation (4) over the observed X-ray band (0.5–2 keV).

Given the observed/derived properties of the lobes ($\gamma = (1.0 \pm 0.2) \times 10^4$, $\nu_{EC} = (2.3 \pm 0.7) \times 10^{19}$ Hz, and see Table 2), the resulting integrated EC flux of the lobes in the 0.5–2 keV band is $(2.5 \pm 0.5) \times 10^{-15}$ erg s^{-1} cm^{-2}. The errors are propagated from uncertainties on $S_{1.4\,\mathrm{GHz}}$, α_r, z and B_{eq}.

6.2 IC scattering in the radio hotspots

To estimate the SSC and EC emission coming from the hotspots, we follow the same procedure as in Section 6.1 and make the same assumptions (i)–(v). Note that for the hotspots we do not assume a cylindrical shape but a spherical shape with radius R. For the SSC emission equation (4) becomes

$$\frac{L_{SSC}}{L_r} = \frac{\nu_{SSC} S_{SSC}}{\nu_r S_r} = \frac{\nu_X S_X}{\nu_r S_r}\left(\frac{\nu_{SSC}}{\nu_X}\right)^{1+\alpha_r} \simeq \frac{u_{syn}}{u_B}, \tag{5}$$

where $\nu_{SSC} = 4/3\gamma^2 \nu_R$ and u_{syn} is the synchrotron photon energy density given in the rest frame of the emitting region by $u_{syn} = (d_L^2 \nu_r S_r)/(R^2 c)$.

Given the observed/derived properties of the hotspots ($\gamma = (4.5 \pm 0.1) \times 10^4$, $\nu_{SSC} = (4 \pm 1) \times 10^{16}$ Hz, $\nu_{EC} = (4 \pm 2) \times 10^{18}$ Hz, and see Table 2), the resulting integrated X-ray flux of the hotspots in the 0.5–2 keV band is $(8 \pm 2) \times 10^{-19}$ erg s^{-1} cm^{-2} for SSC

emission and $(4 \pm 1) \times 10^{-17}$ erg s^{-1} cm^{-2} for EC emission. The errors are propagated from uncertainties on $S_{1.4\,\mathrm{GHz}}$, α_r, z and B_{eq}.

6.3 Thermal gas emission of the group

In Section 5 we have identified a galaxy overdensity around the large radio galaxy. Here we predict the X-ray flux arising from the hot gas of the group in the following way. We scale the total stellar mass of the group $M_* = 10^{12}\,\mathrm{M}_\odot$, estimated in Section 5 via the Voronoi tessellation analysis, to the total mass M_{500} (i.e. the total mass within the radius at which the density is 500 times the critical density) using a robust correlation (Giodini et al. 2009):[1]

$$M_* = A \left(\frac{M_{500}}{5 \times 10^{13}\, h_{72}^{-1}} \right)^{-\alpha}, \quad (6)$$

where $\log_{10} A = 0.3 \pm 0.02$ and $\alpha = 0.81 \pm 0.11$. The resulting total mass of the group is $M_{500} = (2.1 \pm 0.3) \times 10^{13}\,\mathrm{M}_\odot$.

Then, we calculate the X-ray luminosity of the group based on the luminosity–mass L_{X}–M relation obtained via a weak lensing analysis in the COSMOS field (Leauthaud et al. 2010):

$$\frac{M_{200} E(z)}{10^{13.7}\,\mathrm{M}_\odot} = B \left(\frac{L_{\mathrm{X}} E(z)^{-1}}{10^{42.7}\,\mathrm{erg\,s^{-1}}} \right)^{\beta}, \quad (7)$$

where $\log_{10} B = 0.106 \pm 0.0053$, $\beta = 0.56 \pm 0.12$, $E_z = \sqrt{\Omega_{\mathrm{m}}(1+z)^3 + \Omega_\Lambda} = 1.866$ for the cosmology assumed here and $z = 1.168$, and M_{500} is the total mass within a radius encompassing $\geq$500 times the critical density. Note that for the previous calculation M_{200} (the mass within a radius at 200 times the critical density) was used. We can convert M_{500} to M_{200} assuming a Navarro–Frenk–White (NFW) profile with a constant concentration parameter ($c = 5$). This yields an X-ray luminosity of $(1.1 \pm 0.3) \times 10^{43}$ erg s^{-1}. Systematic uncertainty in estimating this number is dominated by the scatter in the stellar mass–total mass relation and is a factor of 2. The resulting X-ray flux in the 0.5–2 keV band, due to hot gas emission of the group, is then $(4 \pm 1) \times 10^{-16}$ erg s^{-1} cm^{-2} in the circular area centred on the radio galaxy and encompassing the radio lobes. When calculating the flux we took into account the L_{X}–T relation to derive the K-correction, following the prescription in Finoguenov et al. (2007). This is consistent with the marginal X-ray detection of the group emission of $14 \pm 12 \times 10^{-16}$ erg s^{-1} cm^{-2}, reported in Section 4.1.

6.4 Comparison of thermal and non-thermal X-ray emission

The observed X-ray flux of the EC-dominated X-ray candidate is compared in Table 2 to the fluxes expected from EC emission of the lobes and hotspots (see also Fig. 8), as well as the thermal emission of the group. From Table 2, one can see that thermal emission of the group is almost an order of magnitude lower than what is observed. Therefore, it is very likely that the observed X-ray emission of our EC-dominated X-ray candidate is mostly produced by the EC process in the lobes with only a small contribution arising from the thermal emission of the group. The sum of the two agrees within the error with the observed emission. Note that the total flux expected from SSC and EC emission of the hotspots is two orders of magnitude smaller than the observed emission and thus can be ignored.

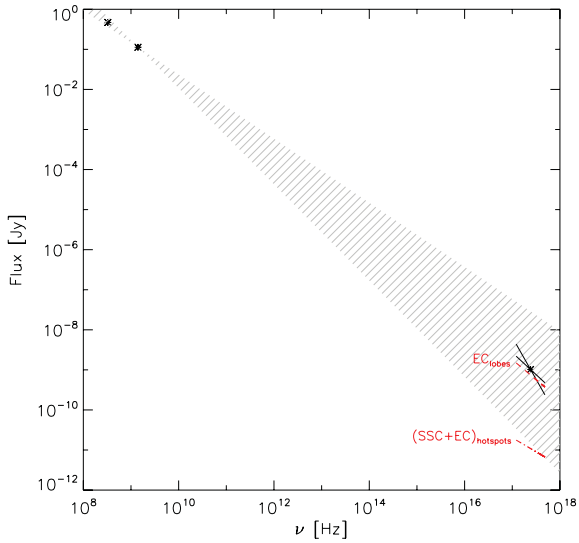

Figure 8. Radio to X-ray spectral energy distribution for the EC-dominated X-ray source with predicted EC emission of the lobes and SSC+EC emission of the hotspots, showing that the measured flux is close to the predicted level for EC emission of the lobes at equipartition. The shaded area illustrates the agreement between the X-ray and radio spectral index as expected for the EC emission.

As presented in Section 4.1, the EC-dominated X-ray candidate clearly shows extended X-ray emission associated only with the lobes of the radio galaxy, and exhibiting a hard X-ray spectrum. Both of these results support the idea that the X-ray emission from the lobes of the radio galaxy predominantly arises from non-thermal IC scattering, rather than thermal group emission.

Based on our optical analysis we have unambiguously associated a galaxy overdensity with the large radio galaxy, i.e. the EC-dominated X-ray candidate. Our results suggest that the distribution of the group galaxies is irregular, i.e. inconsistent with that in relaxed groups or clusters. Furthermore, the optical host of the radio galaxy is found to be a likely merging (double nucleus) source. This resembles the case of 3C 356 at $z = 1.08$ (Simpson & Rawlings 2002). Identifying two subclusters associated with 3C 356, and combining their results with the studies of other powerful radio galaxies, Simpson & Rawlings (2002) suggested that triggering of powerful radio galaxies (at least at $z \sim 1$) is related to galaxy–galaxy interaction which can be coordinated by subcluster mergers. The unrelaxed state of the X-ray lobe overdensity and the double-nucleus host of the radio galaxy seem to be consistent with this scenario.

To date six extended X-ray sources, where the X-ray emission is not dominated by thermal group/cluster emission, at $z > 1$ have been studied in deep X-ray surveys (Geach et al. 2007; Vardoulaki et al. 2008; Tu et al. 2009; Finoguenov et al. 2010). As the CMB energy density is proportional to $(1+z)^4$, the number of extended X-ray sources emitting via IC scattering of CMB photons off the relativistic synchrotron electrons is expected to rise with redshift. This may affect samples of X-ray selected galaxy clusters/groups in deep X-ray surveys, which are regularly based on extended X-ray emission. The contribution of extended non-thermal (EC) sources to such samples is still an open issue. This is addressed in Section 7.

[1] Giodini et al. (2009) combined stellar mass estimates in 118 galaxy groups in the COSMOS field with the weak lensing measurements of the group total mass obtained by Leauthaud et al. (2010).

7 EXPECTED X-RAY COUNTS FROM SYNCHROTRON LOBES

Celotti & Fabian (2004) have studied the contribution of IC-related X-ray emission in the Universe in comparison to that of cluster/group emission. They have shown that IC scattered X-ray emission may dominate that of galaxy clusters/groups above redshifts of 1 and X-ray luminosities of 10^{44} erg s^{-1}. In the 2 deg^2 COSMOS field, searching over all ($\sim$300) extended X-ray sources with X-ray flux $S_{\rm X} \geq 6 \times 10^{-16}$ erg s^{-1} cm^{-2} we have found only one X-ray candidate where the X-ray emission may arise from IC scattering, rather than thermal ICM emission. In the following we compute how many of such sources we would expect in the COSMOS field, and generally in deep X-ray surveys.

First we need to determine the radio LF to use for this analysis. Willott et al. (2001) have generated radio LFs for the two main types of radio AGN – high radio power (predominantly FR IIs; high-excitation sources) and low radio power (predominantly low-excitation FR I and FR IIs). The shape of the LFs as well as their evolution is significantly different for the two (see Willott et al. 2001 for details; see also Smolčić et al. 2009). In order to estimate the number of expected extended X-ray sources on the sky, we start with the radio LF that best describes extended radio AGN, i.e. large radio galaxies.

In deep radio surveys such as the 20 cm VLA-COSMOS, that sample well the low-power radio AGN, the fraction of large radio galaxies relative to unresolved sources (at a resolution of 1.5 arcsec) is only $\sim$10 per cent (Schinnerer et al. 2007; Smolčić et al. 2008, 2009). Furthermore, the mean radio power of these large radio galaxies is $\sim 9 \times 10^{24}$ W Hz^{-1}, i.e. much higher than that for unresolved sources ($\sim 3 \times 10^{23}$ W Hz^{-1}; see e.g. Schinnerer et al. 2007; Smolčić et al. 2009). On the other hand, in shallower surveys that sample predominantly high radio-power AGN, such as e.g. the Third Cambridge Survey (with the average radio luminosity of sources from the 3CRR catalogue of 10^{27} W Hz^{-1} sr^{-1} at 151 MHz), the fraction of large radio galaxies relative to compact sources is substantially higher, i.e. $\sim$95 per cent. Thus, we adopt the LF of powerful radio AGN from Willott et al. (2001) to compute the number of extended X-ray sources on the sky.

We first compute the expected number of extended X-ray sources due to IC scattering of CMB photons (EC) in a 2 deg^2 field (such as COSMOS) by evolving the LF for powerful radio AGN covering the range of 10^{25}–10^{30} W Hz^{-1} (Willott et al. 2001; see also Smolčić et al. 2009). For each redshift we convert the radio luminosities to radio flux assuming a typical spectral index of -0.75. Assuming that the X-ray emission is caused by the EC process, we then compute the expected X-ray flux arising from EC scattering as described in Section 6.1. Given our COSMOS detection thresholds in radio and X-rays, we then calculate the expected number of sources that could be detected above a radio flux of $S_{\rm r} \geq 50$ μJy (VLA-COSMOS detection limit) and an X-ray flux of $S_{\rm X} \geq 6 \times 10^{-16}$ erg s^{-1} cm^{-2} (COSMOS X-ray group detection limit) in a 2 deg^2 field. The differential and integrated number of expected extended EC X-ray sources is shown in Fig. 9. In a field like COSMOS with deep radio and X-ray observations, only one X-ray source where the emission arises from IC-scattered electrons of the CMB is expected. This is consistent with our systematic search for non-thermal extended X-ray sources which yielded only one EC-dominated source (discussed in detail here).

Extending this line of reasoning further we can predict the IC X-ray counts as a function of X-ray flux. Again, evolving the radio LF for powerful radio galaxies (10^{25}–10^{30} W Hz^{-1}; Willott et al. 2001) in a redshift range $0 < z < 6$, we compute the total expected number of EC (extended) X-ray sources per deg^2 of sky. However, unlike in the calculation above, no radio flux limit is imposed here. The differential and cumulative counts are shown in Fig. 10. The peak in the differential source counts (that corresponds to the flattening in the cumulative counts) at $L_{\rm X} \sim 5 \times 10^{-14}$ erg s^{-1} cm^{-2} is due to the shape of the radio LF for powerful radio galaxies that has a strong peak at $L_{20\,\rm cm} \sim 10^{27}$ W Hz^{-1} (see Smolčić et al. 2009). Thus the major contribution to the X-ray counts arises from such galaxies at redshifts 1–3. On the other hand, the number density of $z > 1$ extended X-ray sources in the COSMOS field is $\sim$20 per deg^2. Thus the expected $\sim$0.5 non-thermal X-ray extended source per deg^2 (under the assumption that the underlying radio LF is correct) are not likely to dominate samples of extended (thermal) X-ray sources, i.e. clusters/groups in deep X-ray surveys. To investigate this further, following Finoguenov et al. (2010), we have also computed the source counts for clusters in the redshift range of $1 < z < 3$ (dashed line in Fig. 10). As one can see from Fig. 10 the number of high-z clusters becomes comparable to that of high-z radio galaxies at fluxes exceeding 7×10^{-15} erg s^{-1} cm^2. Thus, EC-dominated X-ray sources may produce a serious contamination for the upcoming eROSITA survey (Predehl et al. 2010).

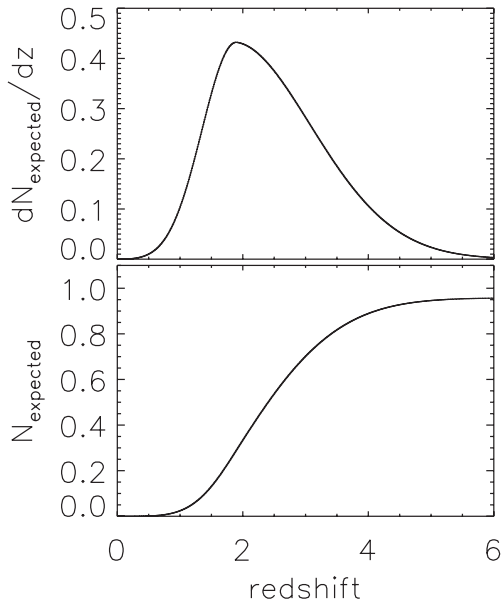

Figure 9. The top (bottom) panel shows the expected differential (cumulative) number of X-ray-emitting lobes in the COSMOS 2 deg^2 field, drawn from the evolving LF of powerful radio AGN (Willott et al. 2001, covering the range of 10^{25}–10^{30} W Hz^{-1}; see text for details).

8 SUMMARY AND CONCLUSIONS

In the COSMOS field we have carried out a systematic search for non-thermal extended X-ray sources, i.e. sources in which the X-ray emission is mostly arising due to IC scattering of CMB photons off electrons in the radio lobes (EC process), rather than thermal emission from the hot gas in the galaxy cluster/group. Based on a concurrence of morphological structures in the radio and X-ray images, we have found only one candidate.

The radio counterpart of our candidate is a large powerful radio galaxy ($L_{\rm r} = 6.7 \times 10^{38}$ W) hosted by a double-nuclei galaxy at $z = 1.1684$. The observed X-ray emission ($S_{0.5-2\,\rm keV} = (3.6 \pm 1.2) \times 10^{-15}$ erg s^{-1} cm^{-2}) is extremely elongated in the direction

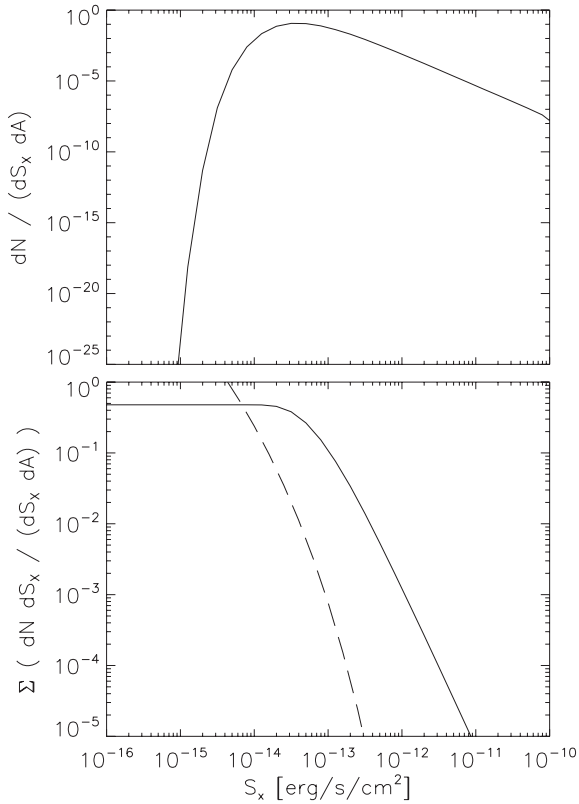

Figure 10. Differential (top panel) and cumulative (bottom panel) number counts (per deg^2) as a function of X-ray flux expected for extended IC X-ray sources (solid lines) and for clusters (dashed line). The radio counts were obtained by evolving the radio LF for powerful (FR II) radio galaxies (Willott et al. 2001, covering the range of 10^{25}–10^{30} W Hz^{-1}; see text for details), while the cluster counts, in the redshift range of $1 < z < 3$, were obtained following Finoguenov et al. (2010).

of the radio lobes (see Fig. 1), suggesting a non-group origin. In order to identify the origin of the X-ray emission in our source, we have performed a detailed analysis of the expected X-ray emission arising from IC emission in the radio lobes, the hotspots, as well as that expected from the group environment of the radio galaxy. We find that external IC emission of the lobes is the dominant process that generates the observed X-ray emission of our candidate (see Fig. 8), with a minor contribution from the intragroup gas of the galaxy group associated with the radio galaxy.

Making use of the radio LF for powerful radio galaxies, we have estimated the expected number of extended non-thermal X-ray sources (due to IC scattering of CMB photons off the synchrotron electrons) on the sky as a function of X-ray flux. In a 2 deg^2 field, such as COSMOS, we expect to find only one such source, consistent with our results. Furthermore, our analysis shows that such sources (in a redshift range $0 < z < 6$ and with radio luminosity between 10^{25} and 10^{30} W Hz^{-1}) are not expected to be a significant contaminant of deep X-ray selected cluster/group catalogues, but they dominate the $z > 1$ cluster counts at the bright end ($S_{\rm X} > 7 \times 10^{-15}$ erg s^{-1} cm^2).

ACKNOWLEDGMENTS

We acknowledge the anonymous referees for their constructive comments. This research is in part funded by the European Union's Seventh Framework programme under grant agreement 229517 and contract PRIN-INAF 2007, by World Premier International Research Center Initiative (WPI Initiative), MEXT, Japan and by KAKENHI No. 23740144. FC acknowledges the Blancheflor Boncompagni Ludovisi foundation and the Smithsonian Scholarly Studies.

REFERENCES

Baldi R. D., Capetti A., 2008, A&A, 489, 989
Baum S. A., Heckman T. M., van Breugel W., 1992, ApJ, 389, 208
Bielby R. M. et al., 2010, A&A, 523, A66
Blundell K. M., Fabian A. C., Crawford C. S., Erlund M. C., Celotti A., 2006, ApJ, 644, L13
Botzler C. S., Snigula J., Bender R., Hopp U., 2004, MNRAS, 349, 425
Bower R. G., Lucey J. R., Ellis R. S., 1992, MNRAS, 254, 601
Bruzual G., Charlot S., 2003, MNRAS, 344, 1000
Celotti A., Fabian A. C., 2004, MNRAS, 353, 523
Croston J. H., Birkinshaw M., Hardcastle M. J., Worrall D. M., 2004, MNRAS, 353, 879
Croston J. H., Hardcastle M. J., Harris D. E., Belsole E., Birkinshaw M., Worrall D. M., 2005, ApJ, 626, 733
Ebeling H., Wiedenmann G., 1993, Phys. Rev. E, 47, 704
Elvis M. et al., 2009, ApJS, 184, 158
Erlund M. C., Fabian A. C., Blundell K. M., 2008, MNRAS, 386, 1774
Fabian A. C., Sanders J. S., Crawford C. S., Ettori S., 2003, MNRAS, 341, 729
Fabian A. C., Chapman S., Casey C. M., Bauer F., Blundell K. M., 2009, MNRAS, 395, L67
Fanaroff B. L., Riley J. M., 1974, MNRAS, 167, 31P
Felten J. E., Rees M. J., 1969, Nat, 221, 924
Finoguenov A. et al., 2007, ApJS, 172, 182
Finoguenov A. et al., 2009, ApJ, 704, 564
Finoguenov A. et al., 2010, MNRAS, 403, 2063
Geach J. E., Simpson C., Rawlings S., Read A. M., Watson M., 2007, MNRAS, 381, 1369
Giodini S. et al., 2009, ApJ, 703, 982
Gobat R. et al., 2011, A&A, 526, A133
Hardcastle M. J., Harris D. E., Worrall D. M., Birkinshaw M., 2004, ApJ, 612, 729
Hasinger G. et al., 2007, ApJS, 172, 29
Henry J. P. et al., 2010, ApJ, 725, 615
Ilbert O. et al., 2009, ApJ, 690, 1236
Johnson O., Almaini O., Best P. N., Dunlop J., 2007, MNRAS, 376, 151
Kataoka J., Stawarz Ł., 2005, ApJ, 622, 797
Kewley L. J., Dopita M. A., Sutherland R. S., Heisler C. A., Trevena J., 2001, ApJ, 556, 121
Koekemoer A. M. et al., 2007, ApJS, 172, 196
Komatsu E. et al., 2011, ApJS, 192, 18
Lamareille F., Mouhcine M., Contini T., Lewis I., Maddox S., 2004, MNRAS, 350, 396
Leauthaud A. et al., 2010, ApJ, 709, 97
Lilly S. J. et al., 2007, ApJS, 172, 70
Lilly S. J. et al., 2009, ApJS, 184, 218
Miley G., 1980, ARA&A, 18, 165
Mocz P., Fabian A. C., Blundell K. M., 2011, MNRAS, 413, 1107
Oklopčić A. et al., 2010, ApJ, 713, 484
Pacholczyk A. G., 1970, Radio Astrophysics. Nonthermal Processes in Galactic and Extragalactic Sources. Freeman & Co., San Francisco
Predehl P. et al., 2010, in Arnaud M., Murray S. S., Takahashi T., eds, Proc. SPIE Vol. 7732, Space Telescopes and Instrumentation 2010: Ultraviolet to Gamma Ray. SPIE, Bellingham, 77320U
Rybicki G. B., Lightman A. P., 1986, Radiative Processes in Astrophysics. Wiley, New York
Salvato M. et al., 2009, ApJ, 690, 1250
Schinnerer E. et al., 2007, ApJS, 172, 46
Schinnerer E. et al., 2010, ApJS, 188, 384

Schwartz D. A., 2002, ApJ, 569, L23
Scoville N. et al., 2007, ApJS, 172, 1
Simpson C., Rawlings S., 2002, MNRAS, 334, 511
Smolčić V., 2009, ApJ, 699, L43
Smolčić V., Riechers D. A., 2011, ApJ, 730, 64
Smolčić V. et al., 2007, ApJS, 172, 295
Smolčić V. et al., 2008, ApJS, 177, 14
Smolčić V. et al., 2009, ApJ, 696, 24
Stawarz Ł., Sikora M., Ostrowski M., 2003, ApJ, 597, 186
Tanaka M., Finoguenov A., Ueda Y., 2010, ApJ, 716, L152
Tu H. et al., 2009, A&A, 501, 475
Vardoulaki E., Rawlings S., Simpson C., Bonfield D. G., Ivison R. J., Ibar E., 2008, MNRAS, 387, 505
Willott C. J., Rawlings S., Blundell K. M., Lacy M., Eales S. A., 2001, MNRAS, 322, 536
Wilson T. L., Rohlfs K., Hüttemeister S., 2009, Tools of Radio Astronomy. Springer-Verlag, Berlin

This paper has been typeset from a TEX/LATEX file prepared by the author.